

# Chapter 2

## Multiple Sensor System Applications, Benefits, and Design Considerations

Millimeter-wave (MMW) and infrared (IR) sensors are frequently used in autonomous multiple sensor systems because their operating frequencies allow relatively compact designs to be realized. Objects that may be difficult to differentiate when only a single sensor is used are often distinguished with a multiple sensor system that exploits several signature-generation phenomena to gather data about the objects and scene of interest. Relatively high probabilities of object detection and classification, at acceptable false alarm levels, can potentially be achieved in inclement weather, high-clutter, and countermeasure environments by using operating frequencies that cover a wide portion of the electromagnetic spectrum. Signatures generated by multiple phenomena also expand the amount of information that can be gathered about the location of vulnerable areas on targets. This is important in smart munition applications where autonomous sensors guide weapons to their targets without operator intervention. Multiple sensor systems are used in civilian applications as well, such as space-based sensors for weather forecasting and Earth resource surveys. Here narrow-band wavelength spectra and multiple receiver configurations, such as active radar transmitters, passive radar receivers, and infrared and visible sensors, provide data about temperature, humidity, rain rates, wind speed, storm tracks, snow and cloud cover, and crop type and maturity. Acoustic, ultrasound, magnetic, and seismic signature-generation phenomena are also used in military and civilian applications, but these are not addressed in detail in this book. However, their data can be fused with those of other sensors using the algorithms and architectures described in later chapters.

A *sensor* consists of front-end hardware, called a transducer, and a data processor. The transducer converts the energy entering the aperture into lower frequencies from which target and background discrimination information is extracted in the data processor. A *seeker* consists of a sensor to which scanning capability is added to increase the field of regard. Seekers may be realized by sensors placed on single- or multiple-axis gimbals, IR detector arrays illuminated by scanning mirrors that reflect energy from a large field of regard, frequency sensitive antenna arrays whose pointing direction changes as the transmitted frequency is swept over some interval, or phased array antennas.

## 2.1 Data fusion applications to multiple sensor systems

One application of sensor and data fusion is in smart munitions that use multiple sensor data to precisely guide warheads and missiles to the desired targets by providing real-time tracking and object classification information, while simultaneously minimizing risk or injury to the personnel launching the weapon. Other applications include tracking of aircraft and missiles with multiple sensors located on spatially separated platforms (ground, air, sea, or space based, or in any combination) or with multiple sensors that are collocated. Spatially separated sensor locations reduce the number of time intervals when targets are blocked from the view of any of the sensors, making tracking data available for larger portions of the target's flight time. The process of combining tracks produced by the sensors involves fusion of the data. When collocated multiple sensors are used, a sensor having a large field of view may be employed, for example, to search a large area. A portion of this area may then be handed off and searched with higher resolution sensors to obtain more accurate tracking or object identification data in the restricted region of interest. The process of conveying the location of the restricted search area to the higher resolution sensor makes use of sensor fusion functionality.

Multiple sensors, responding to different signature-detection phenomena, may also be used to increase the probability that a target signature will be found during a search operation. Objects that may not be recognizable to one sensor under a given set of weather, clutter, or countermeasure conditions may be apparent to the others. Another application of sensors that respond to independent signature-generation phenomena is exemplified by a radar supplying range data to a higher resolution infrared sensor that lacks this information. By properly selecting signal processing algorithms that combine the range data with data from the infrared sensor, new information is obtained about the absolute size of the objects in the field of view of the sensors. The process of combining the multisensor data involves data fusion.

Functions that sensors perform in precision guided weapons applications are summarized in Table 2.1. They are implemented with hardware, software, or combinations of both. Sensor fusion is implicit when multiple sensor data are used to support a function. These sensor functions, with the exception of warhead firing or guidance, carry over into nonmilitary applications. For example, in some intelligent transportation system applications, it is necessary to detect, classify, and track vehicles in inclement weather (such as rain and fog) where the signature contrast between vehicle and background may be reduced or the transmitted energy attenuated.

In addition to the applications discussed above, multiple sensors are used for weather forecasting and Earth resource measurements and surveys. Weather satellites rely on combinations of microwave, millimeter-wave, infrared, and

visible sensors to gather data about temperature and water vapor atmospheric profiles, rain rates, cloud coverage, storm tracks, sea state, snow pack, and wind velocities, to name a few. These applications require the reception of data at as many frequencies and polarizations as there are meteorological parameters to calculate or any combination thereof. The parameters are then determined by inverting the equations containing the measured data and the parameters of interest.<sup>1-7</sup> Satellites such as LANDSAT use visible and IR wavelength sensors to provide information about crop identity and maturity, disease, and acreage planted. Synthetic aperture radar (SAR) is used in still other spacecraft to provide imagery of the Earth, even through cloud cover.<sup>8</sup> SAR provides yet another source of space-based information that can be fused with data from other sensors.

**Table 2.1 Common sensor functions and their implementations in precision guided weapons applications.**

Function	Implementation
Target detection	Multiple threshold levels (may be bipolar) Data processing Image processing
False alarm and false target rejection	Data processing Image processing
Target prioritization	High-resolution sensors Object classification algorithms
Countermeasure resistance	Control of transducer apertures Antenna beamwidth and sidelobes IR pixel size (instantaneous field of view) Receive multiple signatures generated by independent phenomena Data processing Image processing
Target tracking	Seeker hardware Algorithms that fuse tracks and data from multiple sensors and multiple targets
Warhead firing or guidance command to hit desired aim-point	Fine spatial resolution sensors Data processing Image processing

## 2.2 Selection of sensors

Data acquired from multiple sensor systems are more likely to be independent when the operating frequencies of the sensors are selected from as wide an expanse across the electromagnetic spectrum as possible and, furthermore, when the sensors are used in both active (transmit and receive) and passive (receive only) modes of operation as indicated in Figure 2.1. Examples of active sensors are microwave, MMW, and laser radars. Examples of passive sensors include microwave, MMW, and IR radiometers, FLIR (forward looking infrared) sensors,IRST (infrared search and track) sensors, video image processors operating in the visible spectrum, and magnetometers. In selecting the operating frequencies or wavelengths, tradeoffs are frequently made among component size; resolution; available output power; effects of weather, atmosphere, clutter, and countermeasures; and cost. For example, a microwave radar operating at a relatively low frequency is comparatively unaffected by the atmosphere (especially for shorter-range applications), but can be relatively large in size and not provide sufficient spatial resolution. A higher-frequency radar, while smaller in size and of better resolution for the same size aperture, may be higher in cost and more susceptible to atmospheric and weather effects.

Sensors designed for weather forecasting operate at frequencies where energy is either known to be absorbed by specific molecules (such as oxygen to provide

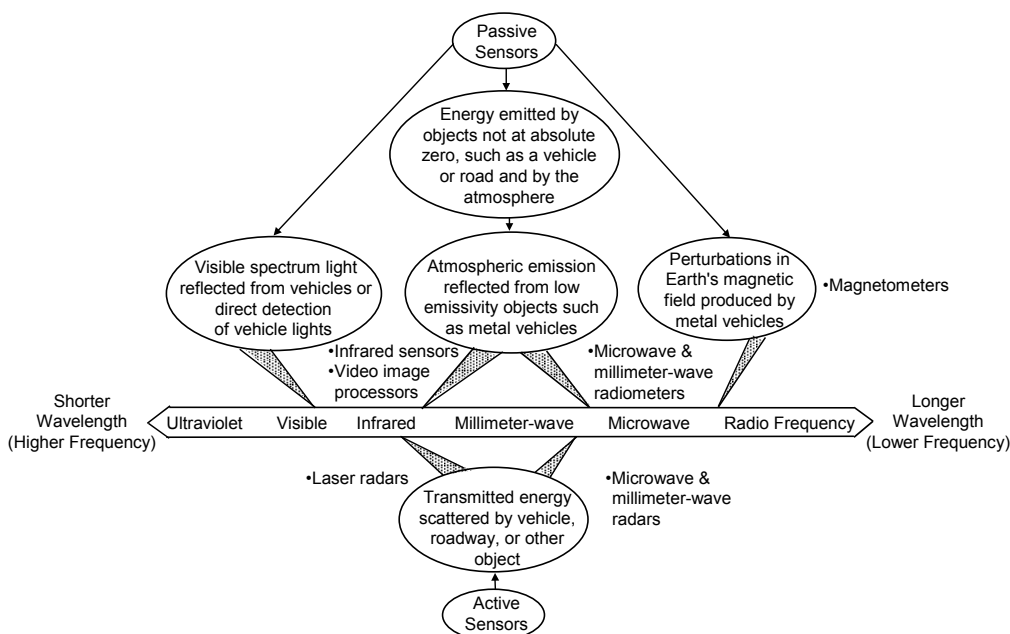


**Figure 2.1** Signature-generation phenomena in the electromagnetic spectrum.

atmospheric temperature profiles or water to provide water vapor profiles) or at frequencies at which the atmosphere is transparent in order to provide measurements at the Earth's surface or at lower altitudes. Other applications, such as secure communications systems, may operate at a strong atmospheric absorption frequency, such as the 60-GHz oxygen complex, to prevent transmission over long distances and to make interception of the information difficult.

Radar sensors operate within frequency bands that are identified by the letter designations shown in Table 2.2. Frequencies in K-band and below are usually referred to as microwave and those at Ka-band and above as millimeter wave.

**Table 2.2 Radar spectrum letter designations.**

<b>Letter</b>	<b>Frequency (GHz)</b>	<b>Free Space Wavelength (mm)</b>
L	1 to 2	300 to 150
S	2 to 4	150 to 75.0
C	4 to 8	75.0 to 37.5
X	8 to 12	37.5 to 25.0
Ku	12 to 18	25.0 to 16.6
K	18 to 26.5	16.6 to 11.3
Ka	26.5 to 40	11.3 to 7.5
Q	33 to 50	9.1 to 6.0
U	40 to 60	7.5 to 5.0
V	50 to 75	6.0 to 4.0
E	60 to 90	5.0 to 3.3
W	75 to 110	4.0 to 2.7
F	90 to 140	3.3 to 2.1
D	110 to 170	2.7 to 1.8
G	140 to 220	2.1 to 1.4

IR sensors operate over spectral regions in the near-, mid-, and long-wavelength IR spectral bands that correspond roughly to 0.77 to 1.5  $\mu\text{m}$ , 1.5 to 6  $\mu\text{m}$ , and 6 to 40  $\mu\text{m}$ , respectively. These bands are usually restricted even further with spectral filters to maximize the response to particular object or molecular signatures and eliminate false returns from the surrounding atmosphere and background.

Active sensors such as MMW radars operate in monostatic and bistatic configurations. In the monostatic mode, the transmitter and receiver are

collocated and the receiver processes energy that is backscattered from objects in the field of view of the antenna. In the bistatic mode, the transmitter and receiver are spatially separated. Here energy is scattered toward the receiver antenna by objects as shown in Figure 2.2. When the bistatic angle  $\beta$  is equal to zero, the configuration reverts to the monostatic case. Bistatic radars do not enjoy as many applications as monostatic radars. They do find use, however, in applications requiring detection and tracking of stealth targets, air-to-ground attack scenarios, satellite tracking, semiactive tracking of missiles, and passive situation assessment.<sup>9</sup>

In the monostatic and bistatic MMW radar configurations, the received signal contains information about scatterer size and location as illustrated in Figure 2.3. IR laser radars provide similar information but at higher resolution, due to their shorter wavelength. However, IR laser radars are subject to greater atmospheric attenuation and an inability to search large areas in a short time. In addition to scatterer size, shape, and location, the energy received by laser radar is also responsive to the differences in reflectance between the objects and their backgrounds. This added discriminant can assist in differentiating targets from backgrounds and other objects.<sup>10</sup>

The inverse relation of sensor resolution to wavelength is depicted in Figure 2.4. In this illustration, the apertures and effective range of the sensors are kept constant at 8 inches (20 cm) and 5 km, respectively, as the operating frequency varies from microwave through visible.

IR passive sensors, such as radiometers, respond to the apparent temperature difference between target and background as indicated in Figure 2.3. The apparent temperature depends on the absolute temperature of the object in the field of view of the radiometer and on the emissivity of the object in the IR spectral band of interest. Temperature sources in the sensor itself that emit energy into the aperture of the sensor also affect the apparent temperature. FLIR andIRST sensors are other types of passive IR devices. FLIRs are primarily used

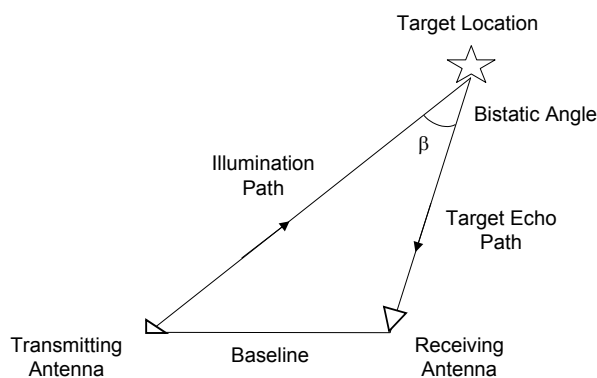


**Figure 2.2 Bistatic radar geometry.**

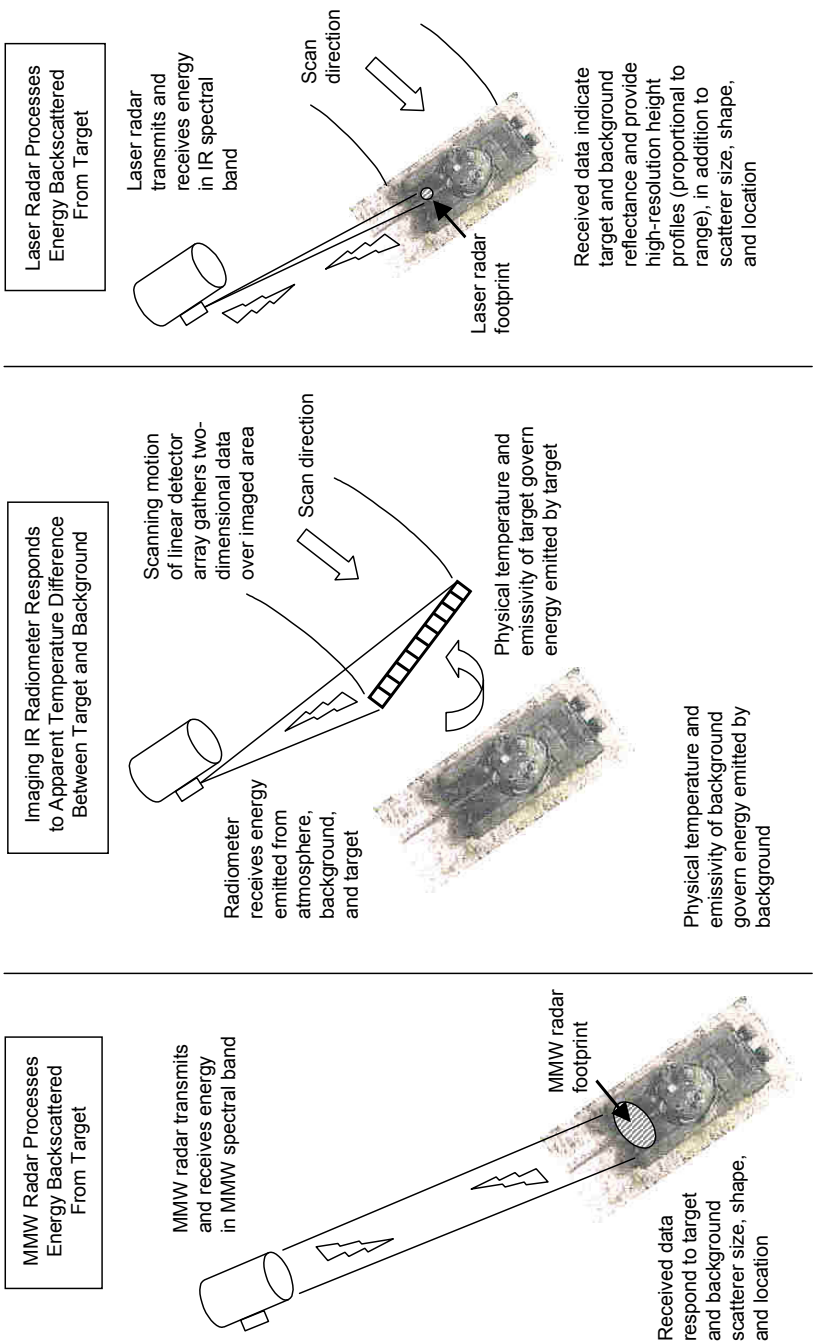
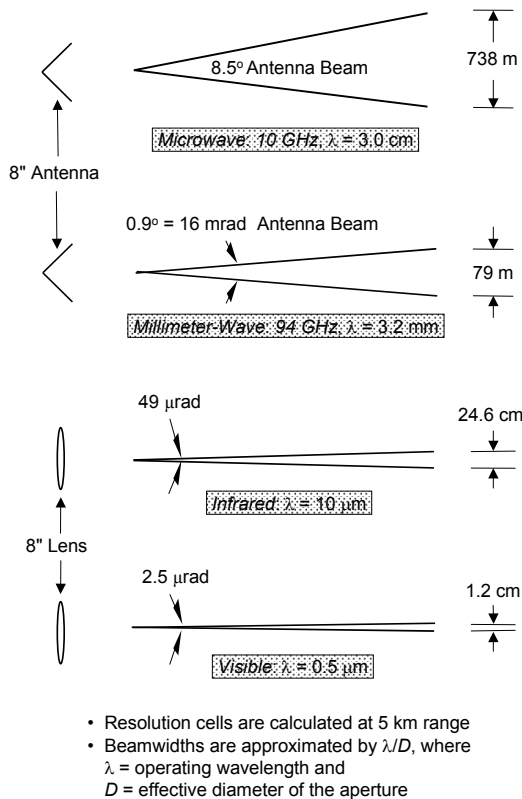


Figure 2.3 Active and passive sensors operating in different regions of the electromagnetic spectrum produce target signatures generated by independent phenomena.



**Figure 2.4 Sensor resolution versus wavelength.**

to provide high-resolution imagery of a scene, whileIRSTs are primarily used to locate a “hot” area on an object and thus track it. Design parameters that optimize the performance of FLIRs, such as a small instantaneous field of view, may hinder the performance ofIRSTs that require a small noise-equivalent temperature difference and hence a larger instantaneous field of view.<sup>11–13</sup> Accordingly, one sensor design may not be optimal for all applications.

Millimeter-wave radiometers, not shown in Figure 2.3, behave in a similar manner to the IR radiometer. They respond to the absolute temperature of the object and its emissivity at the MMW operating frequency of the receiver. Since metal objects have low emissivity and hence high reflectivity at MMW frequencies, their passive signatures are mainly due to (1) reflection of the downwelling component of atmospheric energy from the metal and (2) emission from the upwelling component of energy produced by the background and atmosphere as described by radiative transfer theory in Appendix A.

Cost and sensor performance goals in military applications are influenced by the value of the target the sensor helps defeat. Sensors designed to defeat low-value targets, such as tanks, trucks, and counterfire batteries, are generally of low cost



(several thousand to tens of thousands of dollars), while sensors designed for high-value targets such as aircraft, ships, and bridges can cost hundreds of thousands of dollars. One of the goals of multiple sensor systems is to reduce the cost of smart munitions and tracking systems, whether for the low- or high-value target. This can be achieved by using combinations of lower cost sensors, each of which responds to different signature-generation phenomena, to obtain target classification and tracking data previously available only with expensive, single phenomenon-oriented sensors. Modern missiles and bombs may also incorporate Global Positioning System (GPS) receivers to update their trajectory by fusing the GPS data with data from onboard sensors.

An example of a multiple sensor system that can support automatic target recognition (ATR) is shown in Figure 2.5. For illustration, MMW radar, MMW radiometer, and passive and active IR sensors are shown. In this sensor-level fusion configuration, each sensor processes its data with algorithms that are tailored and optimized to the received frequency band, active or passive nature of the sensor, spatial resolution and scanning characteristics, target and background signatures, polarization information, etc. Results of the individual sensor processing are forwarded to a fusion processor where they are combined to produce a validated target or no-target decision.

If target track estimation is the desired output of the multiple sensor system, then another method of combining the sensor data proves to be more optimal in producing accurate tracks in many applications. In this configuration, called central-level fusion, minimally processed sensor data are associated in the fusion processor. Correlated data are combined to form tracks and estimate future positions of the targets as explained in Chapter 3.

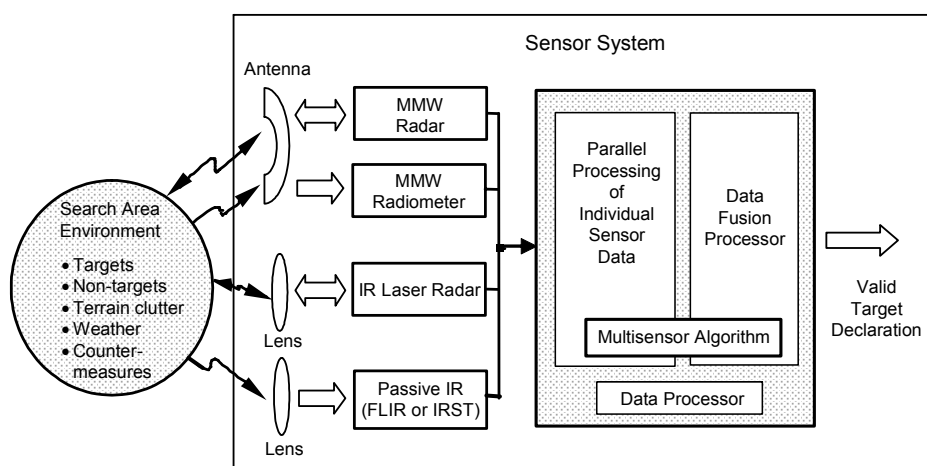


**Figure 2.5** Sensor fusion concept for ATR using multiple sensor data.

## 2.3 Benefits of multiple sensor systems

A quantitative argument can be made for the use of multiple sensor systems as illustrated in Figure 2.6. The lower curve gives the detection probability for a single radar sensor as a function of signal-to-noise ratio when the false alarm probability is equal to  $10^{-6}$ . The detection probability of 0.7 is adequate when the signal-to-noise ratio is nominal at 16 dB. But when the target signature is reduced and the signal-to-noise ratio decreases to 10 dB, the detection probability falls to 0.27, generally not acceptable for radar sensor performance.

If, however, the radar is one of three sensors that detect the target, where each sensor responds to unique signature-generation phenomena and does not generally false alarm on the same events as the others, then the false alarm rejection can be distributed among the three sensors. The system false alarm probability of  $10^{-6}$  is recovered later in the fusion process when the data are combined, for example, with an algorithm such as voting fusion that incorporates sensors operating in series and parallel combinations. When the false alarm rejection can be divided equally among the sensors, the radar performance is given by the upper curve marked with the  $10^{-2}$  false alarm probability. Now the nominal target signature yields a detection probability of 0.85, but even more importantly, the reduced-signature target (with signal-to-noise ratio 10 dB) yields

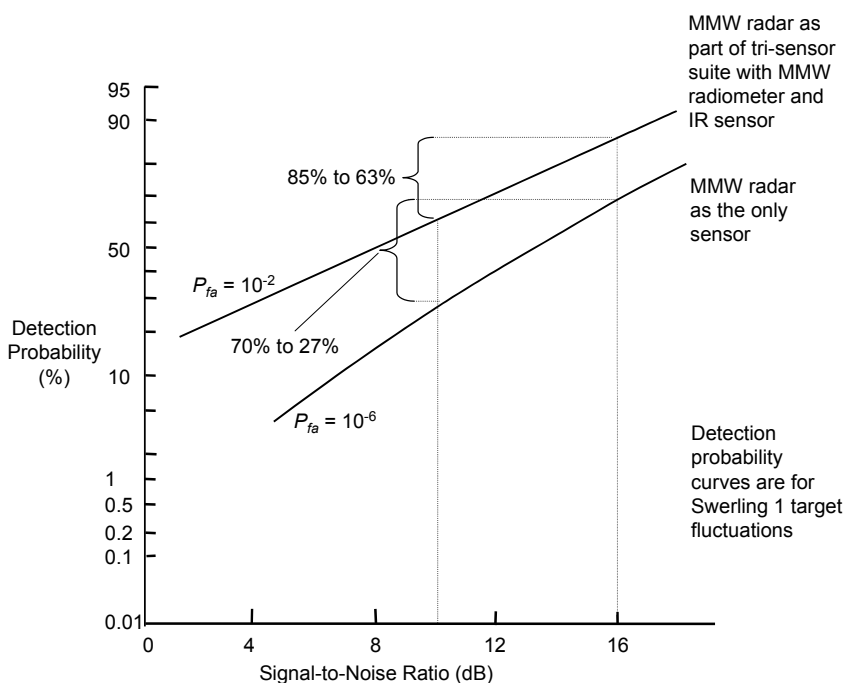


**Figure 2.6 Multiple sensor versus single sensor performance with suppressed target signatures.**

a detection probability of 0.63, which is two and a third times greater than before. Thus, multiple sensors allow the false alarm rejection to be spread over the signature acquisition and signal processing capabilities of all the sensors and the data combining capabilities of the fusion algorithm. This architecture potentially lets each sensor operate at a higher false alarm probability and increases the detection probability of the sensors especially when target signatures are suppressed.

An example of the object discrimination capabilities provided by combining active and passive MMW sensor data is shown in Figure 2.7. Examination of the truck top and shingle roof signatures (on the left of the figure enclosed by dashed lines) shows that it is difficult to tell whether the object is a truck or a roof with only radar data, as both have about the same radar cross section and, hence, relative radar backscatter returns. If a radiometer is added to the sensor mix the difference in the two objects' signatures stands out as shown on the vertical target/background temperature contrast scale. Conversely, if only a radiometer is available, it is difficult to discern an asphalt road from a truck as shown in the dashed region on the right of the figure. However, the radar now adds the discriminating signatures, making object differentiation possible.<sup>14</sup>

Multiple sensors also have the ability to act in a synergistic manner in high-clutter environments and inclement weather. A sensor, such as MMW radar that may be hampered by the high clutter of dry snow, is aided in detecting targets by a passive sensor that is not similarly affected. However, the MMW radar augments an IR sensor that may be impaired by dust or clouds in detecting targets under these conditions.

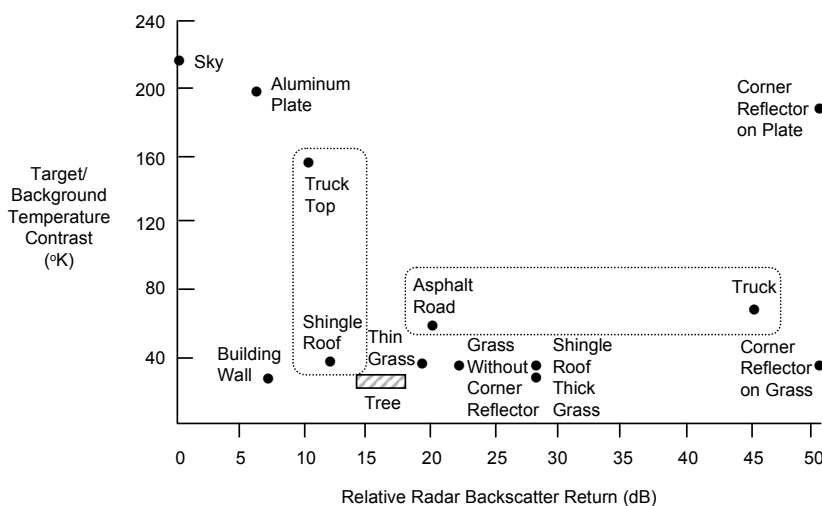


**Figure 2.7 Target discrimination with MMW radar and radiometer data.**

Another example of sensor synergy occurs through the information multiple sensors provide about the location of a potential target's vulnerable area. A passive MMW radiometer supplies data to compute the centroid of the object that can be used as a potential aim-point location. A high-resolution FLIR can provide data to locate the boundary of an object and a region of warmer temperatures within that area. With suitable knowledge about the targets, the warmer region can be inferred to belong to the area over the engine, which is an ideal aim-point. This imagery, as well as the passive MMW centroid data, allows the aim-point to be located within the boundary of the object and avoids the pitfalls of simple hot-spot detection, which can declare a "false aim-point" (e.g., from tracking hot exhaust gases) located outside the physical area of the target.

Benefits from multiple sensor systems also accrue from their ability to defeat countermeasures deployed to make a sensor ineffective either by jamming or by mimicking target signatures that deflect a sensor-guided missile away from the true target track. Multiple sensors either completely or partially defeat these countermeasures by exploiting target signature phenomena that are not countered or by driving up the cost of the countermeasure by requiring it to be more complex to replicate target signatures over a wide spectral band in the active and passive signature domains.

## **2.4 Influence of wavelength on atmospheric attenuation**

Atmospheric attenuation is produced by two phenomena—absorption and scattering. Absorption is dependent on the frequency of operation and the gases and pollutants that are present. Scattering is dependent on the size, shape, and dielectric constant of the scattering objects and the wavelength of the incident energy. Atmospheric constituents such as oxygen, water vapor, and carbon dioxide play a dominant role in determining MMW and IR attenuation. The internal energy states of these molecules define frequencies at which the molecules absorb energy, thus creating frequency bands of high attenuation. These regions of the electromagnetic spectrum may be used to broadcast short-range communications that are intended to be difficult to intercept and to gather information used for weather forecasting and cloud top location. Relatively low absorption exists at still other portions of the electromagnetic spectrum called windows. Sensors that operate at these frequencies can propagate energy over greater distances for long-range target detection and for Earth resource monitoring. Weather-related obscurants such as rain, fog, and snow add to the absorption and scattering experienced under clear weather conditions and further limit sensor performance. Models that adequately predict atmospheric absorption and scattering in the MMW and IR spectra may be used when measured data are not readily available at specific frequencies or atmospheric conditions. In the microwave and millimeter-wave portions of the electromagnetic spectrum, atmospheric attenuation generally increases as the operating frequency increases.

In the infrared portion, attenuation is a strong function of the gases and pollutants that are present.

The higher resolution IR and visible sensors suffer greater performance degradation from the atmosphere, as seen in Figure 2.8. The curve with many peaks and valleys in attenuation corresponds to 1 atm of pressure at a temperature of 20°C and water density of 7.5 g/m<sup>3</sup>. The window frequencies in the MMW spectrum, denoted by absorption minima, occur at approximately 35, 94, 140, 225, and 350 GHz. These windows are the frequencies typically used in sensors designed to detect potential targets. Peak absorption occurs in the microwave and millimeter-wave spectra at approximately 22, 60, 118, 183, and 320 GHz. Absorption at 60 and 118 GHz is due to oxygen, while absorption at the other frequencies is due to water vapor.

The infrared absorption spectra are due to molecular rotations and vibrations that occur in atmospheric molecules. The near-IR wavelength band extending from 0.77 to 1.5  $\mu\text{m}$  is constrained at the upper end by water vapor absorption. The mid-IR wavelength band from 3 to 5  $\mu\text{m}$  is bounded on the lower and upper ends by water vapor absorption. An absorption peak in the middle of the band is due to carbon dioxide. The far-IR band or thermal IR extends from approximately 8 to 12  $\mu\text{m}$  and beyond. The lower wavelength is restricted by water vapor and the upper wavelength by a combination of water vapor and carbon dioxide.

Rain rates of 0.25, 4, 25, and 150 mm/hr affect attenuation as shown in the curves in Figure 2.8. At frequencies below approximately 100 GHz, drizzle (0.25 mm/hr) produces less attenuation on MMW than on IR. In moderate and heavier rain, MMW frequencies of 97 GHz and above are generally subject to similar

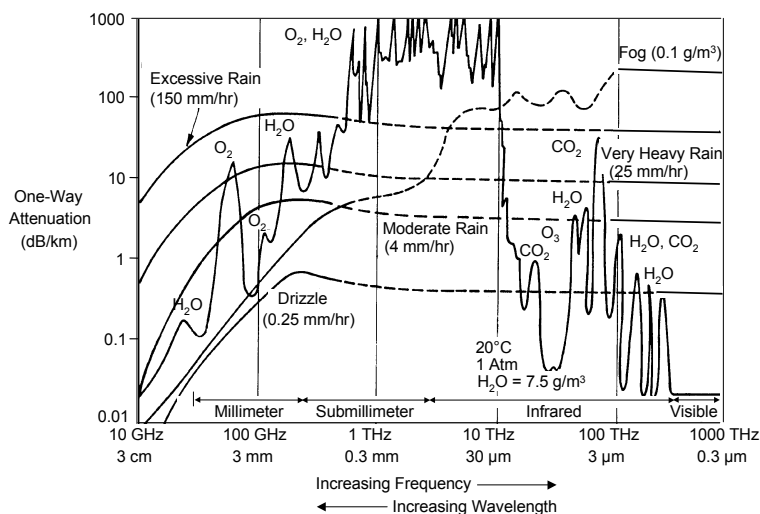


**Figure 2.8 Atmospheric attenuation spectrum from 0.3  $\mu\text{m}$  to 3 cm.**

attenuation as the near IR as the rain rate curves of 4, 25, and 150 mm/hr show. Figure 2.8 also shows that a fog with  $0.1 \text{ g/m}^3$  liquid water content is a greater attenuator of IR energy than MMW energy. Additional data describing the effects of water, in the form of rain and fog, on the propagation of MMW and IR energy are discussed in subsequent sections. Other atmospheric constituents such as carbon dioxide, carbon monoxide, nitrous oxide, oxygen, methane, and ozone are treated by the computer models described in Section 2.14.

Propagation of visible, IR, and MMW energy through snow was studied during the Snow-One and Snow-One-A experiments conducted by the U.S. Army Cold Regions Research and Engineering Laboratories (CRREL) in 1981 and 1982. Transmittance and attenuation data are found in their report and other sources.<sup>15,16</sup> Table 2.3 contains the model for the extinction coefficient for mid- and far-infrared wavelength propagation through snow that was developed by Seagraves and Ebersole using these data.<sup>17</sup> They found that the extinction coefficient could be expressed as a function of only the visible extinction coefficient when the relative humidity was less than or equal to 94 percent. When the relative humidity was larger, making the occurrence of fog more likely, the infrared extinction coefficient was found to be a function of temperature and humidity as well.

The parameters that appear in the model are defined as

$\gamma_{0.55}$  = extinction coefficient at visible wavelengths ( $0.55 \text{ }\mu\text{m}$ ),

$$\frac{\gamma_{0.55}}{V_c} = 0.0233 - 0.0031V_c - 0.0101T + 0.0019H \text{ Np/km}, \quad (2-1)$$

$$\begin{aligned} V_c &= \text{volume concentration of snow in } 10^{-8} \text{ m}^3/\text{m}^3 \\ &= R/v, \end{aligned} \quad (2-2)$$

$R$  = equivalent liquid water precipitation rate,

$v$  = particle settling velocity,

$T$  = surface temperature in  $^{\circ}\text{C}$ ,

$H$  = surface relative humidity in percent, and

$V_i$  = visibility in km

$$= \frac{3.0}{\gamma_{0.55}}. \quad (2-3)$$

**Table 2.3 Extinction coefficient model for snow.** (M.A. Seagraves, and J.F. Ebersole, "Visible and infrared transmission through snow," *Optical Engineering*, Vol. 22, No. 1, 90-93 [Jan.-Feb. 1983].)

Applicable Wavelength	Applicable Humidity	Extinction Coefficient Model
3.0 $\mu\text{m}$	$\leq 94$ percent	$\gamma_{3.0} = 1.21\gamma_{0.55}$ Np/km
3.0 $\mu\text{m}$	$> 94$ percent	$\gamma_{3.0} = \gamma_{0.55} (-0.107T - 0.101H - 0.042V_i + 10.74)$ Np/km
10.4 $\mu\text{m}$	$\leq 94$ percent	$\gamma_{10.4} = 1.18\gamma_{0.55}$ Np/km
10.4 $\mu\text{m}$	$> 94$ percent	$\gamma_{10.4} = \gamma_{0.55} (-0.182T - 0.223H - 0.426V_i + 25.35)$ Np/km

Since the model was derived from data with visibility, temperature, and humidity values in the ranges  $1.2 \text{ km} \leq V_i \leq 7.5 \text{ km}$ ,  $-11.9^\circ\text{C} \leq T \leq 2.0^\circ\text{C}$ , and  $68\% \leq H \leq 100\%$ , respectively, it should be applied with caution elsewhere. The model produces the largest errors in transmittance as compared to measured data when the relative humidity is between 90 and 95 percent, probably because the presence of fog is most in doubt in this region.

## 2.5 Fog characterization

Fogs found over land are of two types, advective fog (formed by cool air passing over a colder surface) typical of coastal regions, and radiative fog (formed by radiative cooling of the Earth's surface below its dew point level) found in inland regions. Advective fogs contain a greater number of large water drops and generally higher liquid water content than radiative fogs.<sup>18</sup> When the size of a particle in fog, cloud, rain, dust, etc. is comparable to the wavelength of the incident energy, the phase of the wave is not uniform over the particle. These phase differences give rise to the observed scattering of energy. Therefore, energy attenuation increases when the ratio of particle size to wavelength approaches unity. Thus, attenuation of shorter wavelengths (higher frequencies) can be greater in advective fogs because of the greater number of large particles and because of the larger liquid water content of the fog.

Optical visibility is commonly used to characterize fog when MMW attenuation is measured. However, optical visibility is hindered by the Mie scattering<sup>19</sup> of light from droplets in the fog, whereas energy at MMW wavelengths is not.\*

\*Mie scattering theory gives the general solution for the scattering of electromagnetic waves by a dielectric sphere of arbitrary radius. Rayleigh scattering, a limiting case of Mie scattering, applies when the wavelength is much larger than the scatterer's diameter.

Therefore, the propagation of millimeter-waves through fog may be significantly greater than it appears to the human eye. Although water density appears to be a more precise measure of fog characterization, the transient nature of a fog makes it difficult to obtain this measure. Hence, the optical visibility characterization persists in comparisons of energy propagation through fog for MMW and IR systems. Visibility metrics are discussed further in Section 2.10.

## 2.6 Effects of operating frequency on MMW sensor performance

Table 2.4 summarizes the relationship of operating frequency on MMW sensor antenna resolution, atmospheric attenuation, and hardware design parameters. With a fixed size aperture, a higher operating frequency reduces the antenna beamwidth and increases resolution. The increased resolution, while increasing pointing accuracy and reducing clutter cell size, may adversely affect the ability to search large areas within an acceptable time. This is due to the inverse relationship between sensor resolution and field of view (higher resolution, smaller field of view), or equivalently, the direct relationship between resolution and scan rate (higher resolution implies higher scan rate to search a given area in the same allotted time). The relation of frequency to atmospheric attenuation has already been introduced through Figure 2.8. Measurement data and models for estimating absorption and scattering of MMW energy by rain and fog are described in the following sections.

**Table 2.4 Influence of MMW frequency on sensor design parameters.**

Parameter	Effect of Higher Frequency
Aperture	Higher gain
Pointing accuracy	Smaller error (standard deviation)
Clutter cell size	Smaller
Attenuation in air	Generally higher
Attenuation and backscatter in rain and fog	Generally higher
Power available	Generally less
Component size	Smaller
Receiver noise figure	Generally higher
Integrated components in production	Less likely

Average power outputs from GaAs IMPATT (Impact Avalanche and Transit Time) diodes operating at 10 GHz and Si IMPATT diodes operating at 100 GHz have increased approximately 3 dB/decade.<sup>20</sup> Solid-state monolithic-microwave integrated-circuit (MMIC) power amplifiers at 35 GHz are produced with 11 W average output power using GaAs high-electron mobility transistor (HEMT) technology. Solid-state MMIC power amplifiers at 94 GHz yield 1 to 2 W

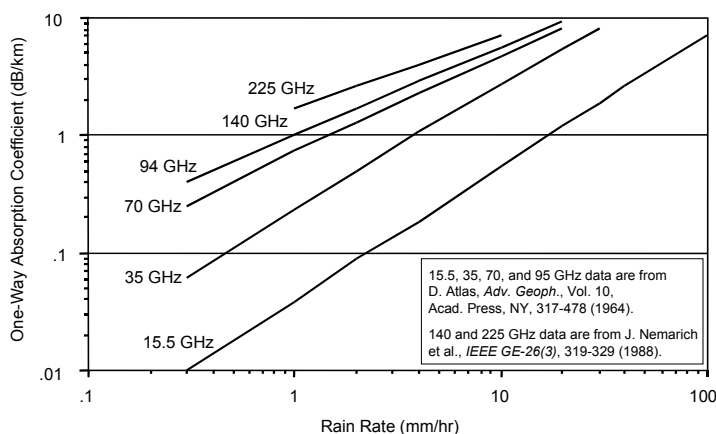


average power using GaAs or InP HEMT technology. Receiver noise figures at 95 GHz are generally larger than at 35 GHz and are dependent on the technology used to manufacture the mixer diodes. Noise figures are larger still at higher frequencies. Since the higher frequency technologies are newer and applications fewer, there are currently less active components available in integrated circuit designs.

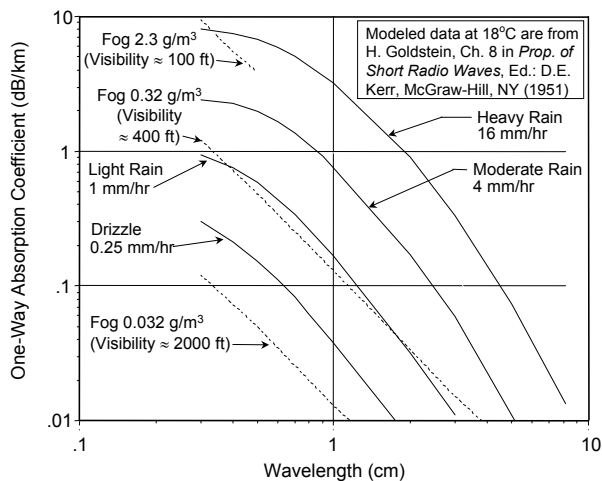
## 2.7 Absorption of MMW energy in rain and fog

Rain affects the propagation of millimeter waves through absorption and backscatter. Figure 2.9 illustrates the one-way absorption coefficients (in decibels per kilometer) for MMW propagation through rain and fog.<sup>21–24</sup> For two-way radar applications, the absorption coefficient is doubled and then multiplied by the range between transmitter and target to get the absorption in decibels by which the energy reaching the sensor is reduced. Figure 2.9(a) shows measured values of the absorption coefficient for 15.5, 35, 70, 94, 140, and 225 GHz as a function of rain rate. Measured absorption data in fog are difficult to gather because of the nonsteady-state character of a fog.

The measured absorption coefficients in rain are predicted from the theoretical model data shown in Figure 2.9(b) by the solid curves corresponding to rain rates of 0.25, 1, 4, and 16 mm/hr. The modeled value of absorption is calculated using the Laws and Parsons drop-size distribution corresponding to the rain rate.<sup>25</sup> This distribution contains the number of droplets with diameters of specific size (0.05 cm to 0.7 cm in increments of 0.05 cm) as a percent of the total rain volume for rain rates of 0.25 to 150 mm/hr. Crane<sup>21,26</sup> found that differences between calculated values of absorption obtained from the Laws and Parsons drop-size distribution and from a large number of observed drop-size distributions were not statistically significant for frequencies up through 50 GHz. At higher frequencies, the drop-size distribution measurement errors in the small drop-size range affected the accuracy of the absorption versus the rain-rate relationship. Therefore, effects produced by different droplet-size models could not be differentiated from effects due to absorption at these frequencies. The agreement of the modeled data with measured values allows the prediction of atmospheric absorption in rain over large regions of the millimeter-wave spectrum and rain-rate variation when measured values are lacking. The data in Figure 2.9(b) may be interpolated to obtain absorption for other values of rain rate.<sup>23</sup>



(a)



(b)

**Figure 2.9 Absorption coefficient in rain and fog as a function of operating frequency and rain rate or water concentration. (a) Measured data, (b) modeled data.**

Because droplet diameters in fog are small compared with millimeter wavelengths, scattering loss is negligible when compared to absorption of millimeter-wave energy by a fog. The one-way absorption coefficient in fog has been modeled as a function of the volume of condensed water in the fog and the operating wavelength of the sensor.<sup>23</sup> The model gives the absorption  $\kappa_\alpha$  as

$$\kappa_\alpha = \frac{0.438 M_W}{\lambda^2} \text{ dB/km}, \quad (2-4)$$

where

$\kappa_\alpha$  = one-way absorption coefficient,

$M_W$  = mass of condensed water per unit volume of air in  $\text{g/m}^3$ , and

$\lambda$  = sensor wavelength of operation in cm.

Equation (2-4) is accurate within 5 percent when  $0.5 \text{ cm} \leq \lambda \leq 10 \text{ cm}$  and when the droplets are extremely small with diameters of the order of 0.001 to 0.005 cm. A value of  $M_W = 1 \text{ g/m}^3$  represents about the maximum water content of most fogs, with the possible exception of heavy sea fogs. In most fogs,  $M_W$  is much less than 1. The FASCODE-1 weather model developed by the U.S. Air Force Geophysics Laboratory simulates<sup>27</sup> two heavy fogs with liquid water contents of 0.37 and 0.19  $\text{g/m}^3$  and two moderate fogs with liquid water contents of 0.06 and 0.02  $\text{g/m}^3$ . (FASCODE is described further in Section 2.14.) For both types of simulated fog, the condensed water mass is less than 1. The modeled absorption data for fog, shown in Figure 2.9(b) by the dashed lines, are plotted from Eq. (2-4).

Ryde and Ryde, as reported by Goldstein, have given an empirical relation between an average  $\overline{M_W}$  and optical visibility in fog, namely,<sup>23</sup>

$$\overline{M_W} = 1660 V_i^{-1.43} \quad (2-5)$$

where  $V_i$  is the optical visibility in feet and  $\overline{M_W}$  is such that in 95 percent of the cases,  $M_W$  lies between  $0.5 \overline{M_W}$  and  $2 \overline{M_W}$ . Such a relation may be useful when more precise values of  $M_W$  are not available.

Calculations made by Richard et al.<sup>28</sup> show that there can be a difference of 8 dB/km in absorption at 140 GHz between advective and radiation fogs at 0.1-km visibility. Earlier measurements by Richer at the Ballistic Research Laboratories found a maximum one-way absorption of 23 dB/km at 140 GHz during a 30-s time period that returned to a lower value of 15 dB/km during the following 30-s interval.<sup>29</sup> The change in absorption was not accompanied by an appreciable change in visibility. The measured 8-dB variation was attributed to an increase in fog density beyond the limits of human visibility or to the condensation of fog into rain along the propagation path.<sup>30</sup>

## 2.8 Backscatter of MMW energy from rain

Backscatter is a volumetric effect. Hence, the rain backscatter coefficient  $\eta$  (in  $\text{m}^2/\text{m}^3$ ) is multiplied by the volumetric resolution cell  $V$  of the radar in cubic meters to obtain the equivalent radar cross section (RCS) of the rain in square

meters. The rain RCS therefore acts as a “pseudotarget” and scatters energy toward the radar receiver that competes with the energy scattered from the real target.

The resolution cell volume  $V$  of the radar is given by

$$V = \pi/4 (R\theta_{az}) (R\theta_{el}) (c\tau/2) \text{ m}^3, \quad (2-6)$$

where

$R$  = range from the radar to the rain resolution cell in meters,

$\theta_{az}, \theta_{el}$  = antenna 3-dB azimuth and elevation beamwidths, respectively, in radians,

$\tau$  = width of the transmitted pulse in seconds, and

$c$  = speed of light in meters/second.

Thus, the RCS of the rain cell is given by

$$\text{RCS} = \eta V \text{ m}^2. \quad (2-7)$$

If the range extent of the resolution cell is limited by a range gate of length  $L$  in meters,  $c\tau/2$  in Eq. (2-6) is replaced by  $L$ .

Rain backscatter coefficient data are shown in Figure 2.10 for linear polarization radars. On the left of the figure are the theoretical backscatter coefficients  $\eta$  as computed by Rozenberg using the Marshall-Palmer drop-size distribution.<sup>31</sup> On the right, are measured values for 9.37 through 70 GHz obtained with a radar that transmitted and received vertical polarization signals as indicated by the V-V polarization notation.

Rozenberg classified rain as precipitation in the form of water drops with diameters in the 0.5- to 7-mm range. Drizzle was classified as precipitation not exceeding 0.25 mm/hr consisting of small droplets with diameters less than 0.5 mm. In the drizzle model of Figure 2.10, the minimum diameter of the drops was 0.1 mm and the maximum diameter was 0.5 mm. The Marshall-Palmer and Laws and Parsons distributions for the number of drops of a given size are nearly equivalent for drop-size diameters greater than 1.0 to 1.5 mm. For backscatter applications where larger drop sizes dominate, the exponential Marshall-Palmer distribution is used.<sup>21</sup> According to Crane, measurements of raindrop size distributions contain large variations for the same location, rain type, and rain rate. Therefore, drop-size distribution models should be regarded as representative of average, rather than individual, rain conditions.<sup>32</sup> The theory for rain backscatter coefficient adequately models the measured values.

If backscatter is large at the selected frequency of operation, a potential solution is to use circular polarization. Figure 2.11 shows that this technique reduces the backscatter by 20 dB at 9.375 GHz and by 18 dB at 95 GHz.<sup>33</sup>

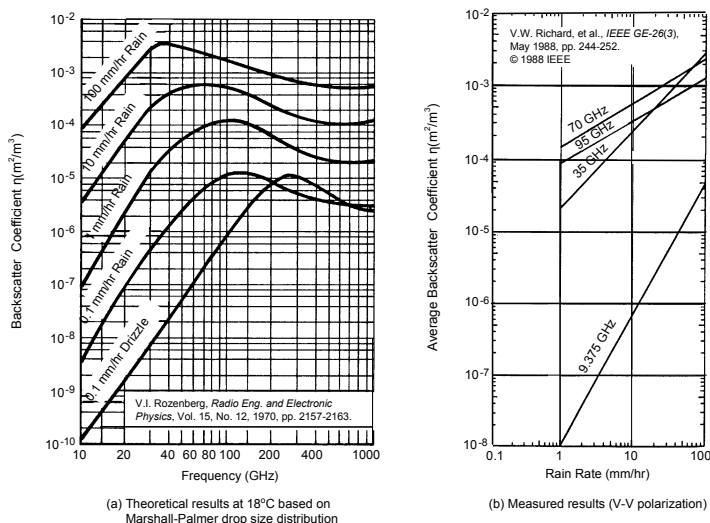


**Figure 2.10** Rain backscatter coefficient as a function of frequency and rain rate.

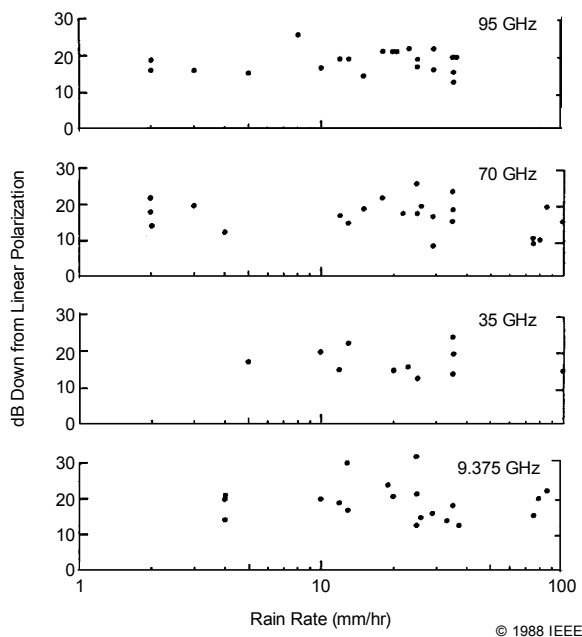


**Figure 2.11** Rain backscatter coefficient reduction by circular polarization. (V.W. Richard et al., *IEEE GE-26* (3), 244-252 [May 1988].)

## 2.9 Effects of operating wavelength on IR sensor performance

IR transmittance through a sea-level atmosphere is shown in Figure 2.12.<sup>34</sup> Unlike the attenuation data given for radar, these data show the transmittance or the percent of energy that is transmitted. The principal permanent atmospheric constituents contributing to the absorption of energy at IR wavelengths are carbon dioxide, nitrous oxide, and methane. Variable constituents include water vapor and ozone. In addition to absorption, IR energy is scattered from molecules and aerosols in the atmosphere. Wavelengths less than 2  $\mu\text{m}$  experience negligible molecular scattering, while scattering from aerosols is a function of the radius of the scatterer divided by the wavelength. Aerosol-type scatterers include rain, dust, fog, and smoke.

Atmospheric transmittance  $\tau_a(\lambda)$  can be modeled by the Lambert-Beer Law<sup>35,36</sup> as

$$\tau_a(\lambda) = \exp [-\gamma(\lambda) R], \quad (2-8)$$

where

$\gamma$  = extinction coefficient or power attenuation coefficient in Np/km and

$R$  = range or path length in km.

Nepers are the natural unit for exponents appearing in an exponential function. Multiplying the extinction coefficient in dB/km by 0.23 converts it into Np/km.

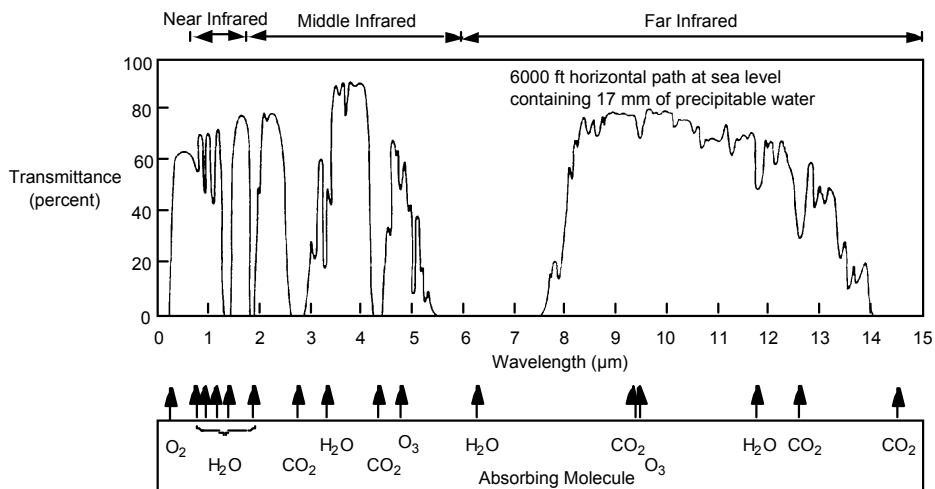


**Figure 2.12 IR transmittance of the atmosphere.** (R.D. Hudson, *Infrared System Engineering*, John Wiley and Sons, NY [1969].)

The extinction coefficient  $\gamma(\lambda)$  is the sum of the absorption and scattering coefficients  $\kappa(\lambda)$  and  $\sigma(\lambda)$ , respectively, and can be written as

$$\gamma(\lambda) = \kappa(\lambda) + \sigma(\lambda). \quad (2-9)$$

Absorption and scattering coefficients, in turn, are sums of molecular and aerosol components denoted by the subscripts  $m$  and  $a$ , respectively, such that

$$\kappa(\lambda) = \kappa_m(\lambda) + \kappa_a(\lambda) \quad (2-10)$$

and

$$\sigma(\lambda) = \sigma_m(\lambda) + \sigma_a(\lambda). \quad (2-11)$$

The extinction coefficient is a complex function of wavelength as may be inferred from Figure 2.12. An expression for the average value of the transmission  $\bar{\tau}_a$  over a wavelength interval  $\lambda_1$  to  $\lambda_2$  is given by

$$\bar{\tau}_a = 1/(\lambda_2 - \lambda_1) \int_{\lambda_1}^{\lambda_2} \exp[-\gamma(\lambda)R] d\lambda. \quad (2-12)$$

The average values of the transmission over a specified wavelength interval are generally obtained from computer-hosted programs such as LOWTRAN, which spans a spectral range of 0 to 50,000  $\text{cm}^{-1}$  (0.2  $\mu\text{m}$  to infinity) with a spectral resolution of 20  $\text{cm}^{-1}$  full width at half maximum (FWHM).<sup>37–39</sup> LOWTRAN and its successor MODTRAN calculate radiance from single and multiple scattering models and path geometries corresponding to space-viewing ground-based sensors, air-to-air scenarios, surface point-to-point paths, and Earth-viewing airborne sensors. Additional information about LOWTRAN and MODTRAN are found in Section 2.14.

## 2.10 Visibility metrics

Two measures of visibility are discussed in this section, the qualitative visibility observed by a human and the quantitative meteorological range.

### 2.10.1 Visibility

Visibility is a qualitative and subjective measure of distance. It is defined as the greatest distance at which it is just possible to see and identify with the unaided eye:

- a dark object against the horizon sky *in the daytime* and
- a known moderately intense light source *at night*.<sup>38</sup>

If the only visibility information available is the visibility metric observed by a human,  $V_{\text{obs}}$ , the meteorological range  $V$  can be estimated as

$$V = (1.3 \pm 0.3)V_{\text{obs}}. \quad (2-13)$$

### 2.10.2 Meteorological range

The quantitative meteorological range metric reported by the U.S. Weather Bureau for many localities can be used to estimate the visual range.<sup>40</sup> It is based on the reduction of apparent contrast produced by atmospheric attenuation at 0.55  $\mu\text{m}$ . The apparent contrast  $C_x$  of a radiation source when viewed at a distance  $x$  is defined as

$$C_x = \frac{R_{sx} - R_{bx}}{R_{bx}}, \quad (2-14)$$

where  $R_{sx}$  and  $R_{bx}$  are the apparent radiance or radiant emittance of the source and background, respectively, when viewed from a distance  $x$ . The units of  $R_x$  are power per unit area. The distance at which the ratio

$$\frac{C_x}{C_0} = \frac{(R_{sx} - R_{bx}) / R_{bx}}{(R_{s0} - R_{b0}) / R_{b0}} \quad (2-15)$$

is reduced to 2 percent is defined as the meteorological range or sometimes the visual range. Equation (2-15) is usually evaluated at  $\lambda = 0.55 \mu\text{m}$ . The subscript 0 refers to the radiance measured at the source and background location, i.e.,  $x = 0$ . Using  $V$  to represent the meteorological range allows Eq. (2-15) to be rewritten to define the meteorological range as

$$\frac{C_{x=V}}{C_0} = 0.02. \quad (2-16)$$

If the source radiance is much greater than that of the background for any viewing distance such that  $R_s \gg R_b$  and the background radiance is constant such that  $R_{b0} = R_{bx}$ , then the meteorological range can be expressed in terms of the apparent radiance as

$$\frac{C_{x=V}}{C_0} = \frac{R_{sV}}{R_{s0}} = 0.02 \quad (2-17)$$

or



$$\ln \left( \frac{R_s V}{R_{s0}} \right) = -3.91. \quad (2-18)$$

The Lambert-Beer law for atmospheric transmittance  $\tau_a(\lambda)$  can be used to relate the extinction coefficient (that includes both absorption and scattering effects) to the meteorological range. Consequently, the atmospheric transmittance is written as

$$\tau_a(\lambda) = \left( \frac{R_s V}{R_{s0}} \right) = \exp [-\gamma(\lambda) R], \quad (2-19)$$

where

$\gamma$  = extinction coefficient or power attenuation coefficient in Np/km

and

$R$  = path length in km.

Upon taking the natural log of both sides of Eq. (2-19) and using Eq. (2-18), we find

$$\gamma(\lambda) = 3.91/V \text{ at } \lambda = 0.55 \text{ } \mu\text{m}. \quad (2-20)$$

Thus, the meteorological range is related to the extinction coefficient through the multiplicative constant of 3.91. This is sometimes referred to as the Koschmieder formula.<sup>38,41</sup>

## 2.11 Attenuation of IR energy by rain

Rain attenuates target-to-background contrast in IR imagery in two ways: first, by introducing an attenuation loss over the signal path to the receiver and second, by cooling the target.<sup>42</sup> A set of atmospheric transmission curves produced by LOWTRAN 6 for rain rates of 0, 1, 10, 30, and 100 mm/hr is shown in Figure 2.13. Here wavenumber is defined as the reciprocal of wavelength, the measurement path is 300 m, surface and dew point temperatures are both equal to 10°C, and the meteorological range is 23 km in the absence of rain. The transmittance curves in the upper portion of the figure apply to the mid- and far-IR spectral bands. The curves in the lower part of the figure apply to the visible and near-IR spectral bands.

## 2.12 Extinction coefficient values (typical)

Typical ranges for the extinction coefficients of atmospheric obscurants are listed in Table 2.5 for the visible, IR, and MMW spectral bands.<sup>43</sup> The extinction coefficient is expressed in units of Np/km. A qualitative correlation between visual range and extinction coefficient is presented in the lower portion of the table.

## 2.13 Summary of attributes of electromagnetic sensors

Resolution, weather, day or night operation capability, clutter, and counter-measures influence the choice of particular electromagnetic sensors for object discrimination and track estimation, as shown in Table 2.6. As frequency is increased, resolution improves and designs are more compact, but degradation by the atmosphere and man-made obscurants increases, while the ability to rapidly search large areas can decrease. Active sensors provide easily acquired range and velocity data, while passive sensors provide stealth operation.

Figures 2.14 through 2.16 illustrate the effect of water fog and dust simulants on the ability of a camera operating in the visible spectrum, mid- and long-wavelength IR imaging sensors, and a 94 GHz MMW radar to generate images of a scene containing a dirt road winding into distant hills. The MMW sensor transmitted a 0.5 W frequency modulated continuous wave signal into an electronically scanned antenna, which scanned a 0.5-degree beam (3-dB beamwidth) over a 30-degree azimuth sector. The tests that produced these images were conducted at the Naval Weapons Center at China Lake, CA during January 2003. The general conclusion reached by the test sponsors was that the airborne obscurants tested did not impact the 94-GHz radar performance in any detectable way. The visible and IR sensors produced imagery that was severely degraded by all of the obscurants (fine, dry, powdered silica clay; fog oil smoke; graphite powder; 5- $\mu$ m diameter water fog droplets) that were dispersed.

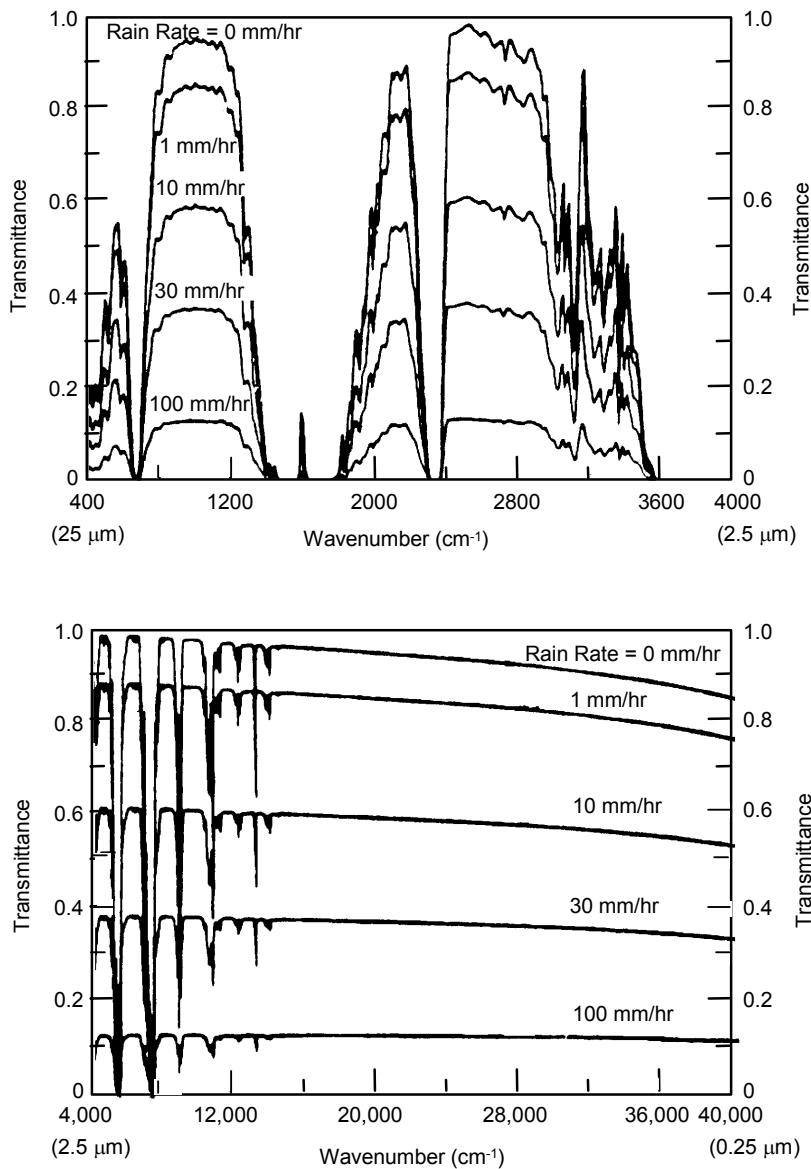


**Figure 2.13 Atmospheric transmittance in rain.** (F.X. Kneizys, et al., *Atmospheric Transmittance/Radiance: Computer Code LOWTRAN 6*, AFGL-TR-83-0187, AFGL, Hanscom AFB, MA 01731 [1983].)

**Table 2.5 Approximate ranges of extinction coefficients of atmospheric obscurants (Np/km).**

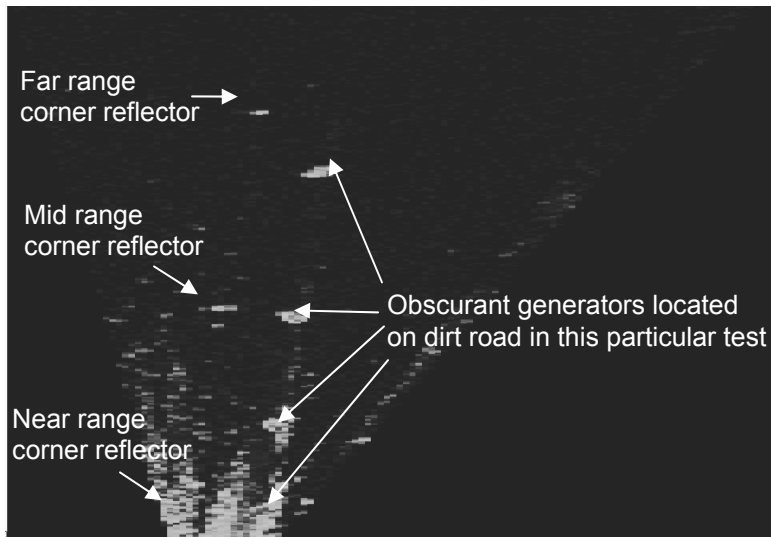
Atmospheric Obscurant	Spectral Region				
	Visible 0.4 to 0.7 $\mu\text{m}$	Mid IR 3 to 5 $\mu\text{m}$	Far IR 8 to 12 $\mu\text{m}$	MMW (35 GHz) 8.6 mm	MMW (95 GHz) 3.2 mm
Gases	Very low: $\cong 0.02$	Low/med: 0.25 to 0.73	Very low/med: 0.03 to 0.8	Very low: 0.02 to 0.06	Very low/low: 0.03 to 0.2
Haze	Low/med: 0.2 to 2.0	Very low/med: 0.02 to 1.0	Very low/low: 0.02 to 0.4	Very low: $\cong 0.001$	Very low: $\cong 0.001$
Fog	High: 2.0 to 20	Very low/med: 1.0 to 20	Med/high: 0.4 to 20	Very low/low: 0.001 to 0.1	Very low/low: 0.01 to 0.4
Rain	Low/med: 0.3 to 1.6	Low/med: 0.3 to 1.6	Low/med: 0.3 to 1.6	Very low/med: 0.05 to 1.0	Low/med: 0.3 to 2.0
Snow	Med/high: 2.0 to 12	Med/high: 2.0 to 12	Med/high: 2.0 to 12	Very low/med: 0.004 to 1.0	Very low/med: 0.03 to 1.0
Dust	Low/high: 0.2 to 4.0	Low/high: 0.2 to 4.0	Low/high: 0.2 to 4.0	Very low: 0.0005 to 0.005	Very low: 0.0005 to 0.005

Extinction Coefficient	Descriptive Term	Visual Range
< 0.1 Np/km	Very low	> 30 km, very clear
0.1 to 0.5 Np/km	Low	6 to 30 km, clear to hazy
0.5 to 2 Np/km	Medium	2 to 6 km, hazy
> 2 Np/km	High	< 2 km, foggy

**Table 2.6 Electromagnetic sensor performance for object discrimination and track estimation.**

Sensor	Advantages	Disadvantages
Microwave/ millimeter- wave radar	All weather Lower frequencies penetrate foliage Large search area Day/night operation Range and image data Velocity data with coherent system	Moderate resolution Not covert Simpler radar designs exhibit more susceptibility to corner reflector decoys and active jammers
Microwave/ millimeter- wave radiometer	Covert imagery All weather Lower frequencies penetrate foliage Large search area Day/night operation	Somewhat less resolution than radar for same aperture Large bandwidth increases susceptibility to jamming Range data, in theory, by performing a maneuver
Infrared imager (FLIR)	Fine spatial and spectral resolution imagery Covert Day/night operation	Affected by rain, fog, haze, dust, smoke Poor foliage and cloud penetration Requires cooled focal plane to maximize signal-to-noise ratio Large search areas require scan mechanism or large detector array Range data by performing a maneuver
Infrared tracker (IRST)	Hot-spot detection Covert target tracking Compact Day/night operation	Same disadvantages as infrared imager
Laser radar	Fine spatial and spectral resolution imagery Range and reflectance data Velocity and track data Can be compact Day/night operation	Affected by rain, fog, haze, dust, smoke Poor foliage penetration Most effective when cued by another sensor to search a relatively small area
Visible imager	Best-resolution imager Covert Technology well understood	Daylight or artificial illumination required Affected by clouds, rain, fog, haze, dust, smoke and any other atmospheric obscurants No foliage penetration No range data



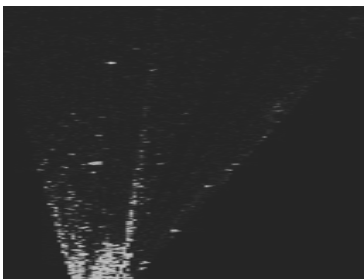
**Figure 2.14** Typical 94 GHz radar backscatter from test area in absence of obscurants.



3-5  $\mu\text{m}$  sensor image.



Visible spectrum image of test area.

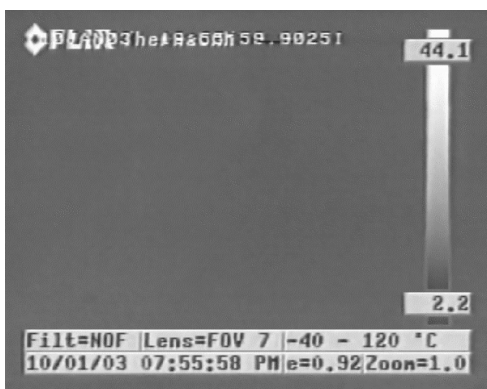


94-GHz radar backscatter.



Visible image corresponding to view seen by 94-GHz radar.

**Figure 2.15** Visible, mid-IR, and 94-GHz sensor imagery obtained during dispersal of water fog. The 3-5  $\mu\text{m}$  and visible spectrum images are obscured where water droplets are present.



3-5  $\mu\text{m}$  sensor image.



8-12  $\mu\text{m}$  sensor image.



Visible image of test area from top of trailer where visible and IR sensors were mounted.



94-GHz radar backscatter.



Visible image corresponding to view seen by 94-GHz radar.

**Figure 2.16** Visible, mid- and far-IR, and 94-GHz sensor imagery obtained during dispersal of graphite dust along road.

## 2.14 Atmospheric and sensor system computer simulation models

The following sections contain descriptions of LOWTRAN, MODTRAN, FASCODE, and EOSAEL. The first three are atmospheric attenuation models. The fourth model analyzes a variety of processes that affect the performance of MMW, IR, visible, ultraviolet, and laser sensors. The material below introduces the phenomena that are treated by the models but is not meant to be a complete user manual for the computer programs.

### 2.14.1 LOWTRAN attenuation model

LOWTRAN 7 (rendered obsolete by MODTRAN 4) calculates atmospheric transmittance, atmospheric background radiance, single-scattered solar and lunar radiance, direct solar irradiance, and multiple-scattered solar and thermal radiance. The spectral resolution is  $20\text{ cm}^{-1}$  (FWHM), taken in  $5\text{-cm}^{-1}$  steps from 0 to  $50,000\text{ cm}^{-1}$ . A single parameter (absorption coefficient) is used to model molecular line absorption and molecular continuum absorption. LOWTRAN also models molecular scattering and aerosol and hydrometer absorption and scattering.

The input parameters for executing LOWTRAN 7 are contained on five main cards and thirteen optional cards. The types of information contained on each card are summarized<sup>39</sup> in Table 2.7.

The user specifies the geographical atmospheric model (from one of six defined by LOWTRAN 7 or from user-generated input), the altitude- and seasonal-dependent aerosol profiles, and the extinction coefficients. The six program-defined geographical atmospheric models are tropical, midlatitude summer, midlatitude winter, subarctic summer, subarctic winter, and the 1976 U.S. standard. Each atmospheric model defines the temperature, pressure, density, and atmospheric gases mixing ratio as a function of altitude. The gases modeled are water vapor, ozone, methane, carbon monoxide, and nitrous oxide. Aerosol profiles and extinction coefficients for the boundary layer (0 to 2 km), troposphere (2 to 10 km), stratosphere (10 to 30 km), and transition profiles from the stratosphere up to 100 km are provided through program-defined models and user-selected inputs. Rain rate, cloud models, wind speed, and meteoric dust extinction coefficients can be varied to tailor the aerosol profiles to the conditions under which the transmission is desired. Table 2.8 contains the characteristics of the rural, urban, maritime, tropospheric, and fog aerosol profiles that are defined by LOWTRAN.<sup>37-39</sup>



**Table 2.7 LOWTRAN 7 input card information.**

Card	Information
1	Specifies one of six geographical-seasonal model atmospheres or a user-specified model; horizontal, vertical, or slant atmospheric path; transmittance or radiance calculation; scattering option
2	Altitude- and seasonal-dependent aerosol profiles and aerosol extinction coefficients, cloud and rain models, wind speed, altitude of surface relative to sea level
2A	Cirrus cloud altitude profile
2B	Vertical structure algorithm of aerosol extinction and relative humidity for low visibility or low ceiling conditions as occur with: (1) cloud/fog at the surface, (2) hazy/light fog, (2') clear/hazy, (3) radiation fog or inversion layer, (4) no cloud ceiling or inversion layer
2C	Additional data for user-defined atmospheric model (if selected on Card 1)
2C1	Additional data for user-defined atmospheric model (if selected on Card 1)
2C2	Additional data for user-defined atmospheric model (if selected on Card 1)
2C3	Additional data for cloud, fog, and rain user-defined atmospheric model (if selected on Card 1)
2D	User-defined attenuation coefficients for any or all four of the aerosol altitude regions (boundary layer, troposphere, stratosphere, above stratosphere to 100 km)
2D1	Conversion factor from equivalent liquid water content ( $\text{g/m}^3$ ) to extinction coefficient ( $\text{Np/km}$ )
2D2	User-defined aerosol or cloud extinction coefficients, absorption coefficients, and asymmetry parameter
3	Geometrical path parameters
3A1	Solar/lunar scattered radiation
3A2	Additional parameters for solar/lunar scattered radiation
3B1	User-defined phase functions
3B2	Additional parameters for user-defined phase functions
4	Spectral range and calculation increment (frequency step size in $\text{cm}^{-1}$ )
5	Recycle parameter to iterate the calculations through the program so that a series of problems can be run with one submission of LOWTRAN

**Table 2.8 LOWTRAN aerosol profiles.**

<b>Aerosol Model</b>	<b>Representative Region</b>	<b>Constituent</b>	<b>Default Visibility*</b>
Rural (0 to 2 km altitude)	Continental areas not directly influenced by urban/industrial aerosol sources	Atmospheric gases and surface dust particles	23 or 5 km
Urban (0 to 2 km altitude)	Modifies rural background by adding aerosols from combustion products and industrial sources	20%/80% mixture of carbonaceous aerosols to rural type aerosols, respectively	5 km
Maritime (0 to 2 km altitude)	Aerosols of oceanic origin	Sea salt particles	User selected or 23 km
Tropospheric (2 to 10 km altitude)	Troposphere with extremely clear conditions and uniform aerosol properties	Rural model constituents without large particles	50 km
Fog 1 (0 to 2 km altitude)	Advection fog	Water droplets	0.2 km
Fog 2 (0 to 2 km altitude)	Radiation fog	Water droplets	0.5 km

\* Visibility refers to the surface meteorological range.

### 2.14.2 FASCODE and MODTRAN attenuation models

Other models available to assess the effects of weather on sensor systems are FASCODE and MODTRAN 4. These are supported by the U.S. Air Force Geophysics Laboratory at Hanscom Air Force Base, Bedford, Massachusetts 01731.<sup>44–51</sup> FASCODE is available from the Geophysics Laboratory via an e-mail request. MODTRAN 4 is available by signing a nondisclosure agreement with the U.S. Air Force and payment of a licensing fee for downloading privileges and support. A CD version of MODTRAN 4 can be obtained from Ontar Corporation once the nondisclosure agreement is signed and fees are paid.<sup>†</sup>

<sup>†</sup> The contact personnel at the Geophysics Laboratory are Gail Anderson: GAnderson@plh.af.mil and Jim Chetwynd: Chetwynd@plh.af.mil. The latest description of MODTRAN 4 and licensing information is available at <http://www-vsbn.plh.af.mil/soft/modtran4.html>. Ontar Corporation's web site is [Ontar.com](http://Ontar.com).

FASCODE models very high altitude ( $>70$  km) and very narrow spectral bands that are applicable to laser-line resolution. FASCODE is useful for extinction dominated by molecular absorption, improving upon the resolution offered by LOWTRAN in this region. MODTRAN was written for moderate resolution calculations that do not require FASCODE. Originally an enhanced version of LOWTRAN 7, MODTRAN contains six additional routines that increase the  $20\text{ cm}^{-1}$  spectral resolution found in LOWTRAN to  $2\text{ cm}^{-1}$  (FWHM) resolution for wavelengths less than 380 nm. Ultraviolet frequencies retain the  $20\text{ cm}^{-1}$  spectral resolution, although future resolution improvements are planned for this region as well.<sup>45</sup> MODTRAN models the molecular absorption by atmospheric molecules as a function of temperature and pressure and provides new capabilities for calculating three absorption band parameters for thirteen molecular species (water vapor, carbon dioxide, ozone, nitrous oxide, carbon monoxide, methane, oxygen, nitric oxide, sulfur dioxide, nitrogen dioxide, ammonia, nitric acid, and oxygen-hydrogen). The absorption band parameters in MODTRAN are temperature dependent and include an absorption coefficient, a line density parameter, and an average linewidth. LOWTRAN 7 uses only the absorption coefficient and molecular density scaling functions to define the absorption band. MODTRAN 4 offers an improved multiple scattering model for more accurate transmittance and radiance calculations that facilitate the analysis of hyperspectral imaging data.<sup>52</sup> Sets of bi-directional radiance distribution functions (BRDFs) have been provided to support surface scattering distributions other than Lambertian.

MODTRAN has been successfully compiled and executed under UNIX using a FORTRAN 77 compiler and in IBM-compatible personal computers using a binary source code with a Lahey F77L32 compiler. All the usual LOWTRAN options such as aerosol profiles, path selection, multiple scattering models, and user-specified inputs have been maintained in MODTRAN.

The input data sequence for MODTRAN is identical to LOWTRAN 7 except for one modification to Card 1 and two modifications to Card 4. A logical parameter MODTRN has been added to the front end of Card 1 to act as a switch. When set to F (false), it causes LOWTRAN 7 to execute. When set to T (true), it activates MODTRAN. The input to Card 4 has been changed to integer format and a resolution parameter IFWHM added as the last entry on the card. IFWHM is only read if MODTRN is true, specifying the full width at half maximum of an internal triangular slit function that determines the  $2\text{ cm}^{-1}$  spectral resolution of the program.

### 2.14.3 EOSAEL sensor performance model

One of the more comprehensive models for analyzing a variety of physical processes that affect the performance of MMW and IR sensors, as well as those that operate in the visible, ultraviolet, and on 53 laser lines, is EOSAEL (Electro-

Optical Systems Atmospheric Effects Library).<sup>53,54</sup> The aspects of electromagnetic energy propagation and defense application scenarios addressed by the model are:

- spectral transmission and contrast transmission;
- multiple scattering;
- sensor performance;
- transport and diffusion;
- turbulence effects on imaging;
- high-energy laser propagation;
- radiative transfer;
- thermal contrast;
- generation of battlefield obscurants;
- climatology for 47 nonoverlapping climatic regions.

EOSAEL 92 (the latest version) software contains 27 modules that are divided into nine categories: gaseous transmission, natural aerosols, battlefield aerosols, radiative transfer, laser propagation, waves and acoustic, target acquisition, decision aides, and support. The modules are more engineering oriented than based on first principles. The EOSAEL development philosophy was to include modules that give reasonably accurate results, while minimizing computer time, for conditions that may be expected on a battlefield. The modules can be executed under the control of an executive routine or in a stand-alone mode. Versions that allow the program to run on a variety of computers are available in FORTRAN 77.

The modules and functions contained in EOSAEL 87, Version 2 (March 1990) are listed in Table 2.9. Three modules of particular interest are the previously discussed LOWTRAN and NMMW (both found in the gases category) and TARGAC. NMMW models the effects of atmospheric gases on MMW sensors. TARGAC, in the target acquisition and system performance category, is built into the FLIR performance model developed by the U.S. Army Center for Night Vision and Electro-Optics (CNVEO).<sup>13,55-57</sup> The FLIR performance model describes the relation of the target-to-background contrast temperature to the sensor resolution and the range between the sensor and target at which the target can be detected, classified, or identified. Ontar Corporation supplies a demonstration FORTRAN source code version of EOSAEL 87, Version 2 (March 1990) on a CD at no charge. The newer EOSAEL 92 can be procured from Ontar as well.

## 2.15 Summary

The attributes of active and passive sensors in the microwave, millimeter-wave, and infrared portions of the electromagnetic spectrum have been enumerated to illustrate the advantages they bring to a high-performance, multisensor suite in defense and civilian applications. The selection of MMW and IR sensor operating frequencies has an impact on resolution, hardware availability and specifications, compatibility with the expected signatures from the objects of interest, and the backgrounds in which the sensors operate. In civilian applications, the longer wavelength microwave and millimeter-wave sensors penetrate clouds and provide data used in weather forecasting, pollution and Earth resource management, and land-use monitoring. Multispectral IR imagery provides information about land cover and geological features, cloud cover, river expansion from floods, and changes in the ocean ecosystem. The relatively good performance of the active mode microwave and MMW sensors in inclement weather and various countermeasures can be used to complement an IR sensor to provide reliable target detection, range, and tracking for military applications. The higher resolution IR sensors provide imagery for classifying potential military targets and improving the selection of a missile impact point.

Measured data and models were presented for calculating atmospheric absorption and backscatter of MMW and IR energy in clear weather, rain, and fog. Attenuation of MMW and IR energy may be modeled using an extinction coefficient that contains terms to account for absorption and scattering. The modeled data generally agree with measured data and, therefore, can be used to predict sensor performance when actual absorption and backscatter measurements are not available. Some of the models only address atmospheric effects, while others, such as EOSAEL, model more complex problems and scenarios.

**Table 2.9 EOSAEL 87 modules and their functions.**

Category	Module	Valid Range	Function
Gaseous Transmission	LOWTRAN	0.25 to 28.5 $\mu\text{m}$	Calculates atmospheric transmittance, radiance, and contrast due to specific molecules at 20 inverse cm spectral resolution on a linear wave-number scale
	LZTRAN	Visible to far IR (0.5 to 11.0 $\mu\text{m}$ )	Calculates transmission through atmospheric gases at specific laser frequencies for slant or horizontal paths
	NMMW	10 to 1000 GHz (0.3 to 30.0 mm)	Calculates transmission, backscatter, and refractivity due to gaseous absorption, fog, rain, and snow

**Table 2.9 EOSAEL 87 modules and their functions (continued).**

Category	Module	Valid Range	Function
Natural Aerosols	XSCALE	0.2 to 12.5 $\mu\text{m}$	Calculates fog and haze transmission for horizontal or slant paths and rain and snow transmission for horizontal paths
	CLIMAT	Not applicable	Provides values of meteorological parameters for select European, Mideastern, Korean, Alaskan, Scandinavian, Central American, Indian, SE Asian, South American, and Mexican locales
	CLTRAN	0.2 to 2.0 $\mu\text{m}$ 3.0 to 5.0 $\mu\text{m}$ 8.0 to 12.0 $\mu\text{m}$	Calculates slant path transmission through six cloud types
	COPTER	0.4 to 0.7 $\mu\text{m}$ 3.0 to 5.0 $\mu\text{m}$ 8.0 to 12.0 $\mu\text{m}$ 0.3 to 30.0 mm	Calculates effects of loose snow or dust lofted by helicopter downwash
Battlefield Aerosols	COMBIC	0.4 to 1.2 $\mu\text{m}$ 3.0 to 5.0 $\mu\text{m}$ 8.0 to 12.0 $\mu\text{m}$ and 94 GHz (3 mm)	Calculates size, path length, concentration, and transmission through various smokes and artillery or vehicular dirt and dust particles
	SABRE	Not applicable	Calculates effects of terrain on wind flow and smoke screens
	KWIK	Not applicable	Provides a placement and number of smoke munitions necessary to produce a screen that reduces the probability of target detection to a given level
	GRNADE	0.4 to 1.2 $\mu\text{m}$ 3.0 to 5.0 $\mu\text{m}$ 8.0 to 12.0 $\mu\text{m}$ and 94 GHz (3 mm)	Models obscuration produced by tube-launched grenades used in self-screening applications
	FITTE	0.4 to 12.0 $\mu\text{m}$	Calculates dimensions of and transmittance through plumes from burning vegetation and vehicles
	MPLUME	Not applicable	Calculates performance degradation of target designation systems by missile smoke plumes
Radiative Transfer	FACLOUD	Any wavelength included in the phase function file PFNDAT*	Calculates beam transmittance, path radiance, and contrast transmittance through a homogeneous ellipsoidal cloud

**Table 2.9 EOSAEL 87 modules and their functions (continued).**

Category	Module	Valid Range	Function
Radiative Transfer continued	OVRCT	Any wavelength	Calculates beam transmittance, path radiance, and contrast transmittance along an arbitrary line of sight under an overcast sky
	MSCAT	Any wavelength included in the phase function file PFNDAT	Calculates multiple scattering of a laser beam into a detector from an ellipsoidal aerosol cloud
	ASCAT	Any wavelength included in the phase function file PFNDAT	Calculates effects of multiple scattering for transmissometer and lidar configurations
	ILUMA	Photopic	Predicts natural illumination under realistic atmospheric conditions
	FASCAT	0.55 and 1.06 $\mu\text{m}$	Determines path radiance and contrast effects
	GSCAT	Visible	Determines path radiance effects
	LASS	Visible	Determines the effectiveness of smoke screens deployed against large fixed and semifixed installations
Laser Propagation	REFRAC	$\approx 0.4$ to $\approx 20.0$ $\mu\text{m}$	Calculates the amount of curvature a ray of light experiences as it passes over a complex terrain surface
	IMTURB	$<14$ $\mu\text{m}$	Predicts the effects of laser propagation through optical turbulence in the weak fluctuation regime
	NOVAE	$<14$ $\mu\text{m}$	Calculates linear and nonlinear effects on high-energy laser beam propagation from clear air, smokes, and aerosols
Target Acquisition and System Performance	TARGAC	Visible to mid-IR	Evaluates the combined atmospheric and system effects to determine the range for target detection and classification
	RADAR	0.1 to 350 GHz	Calculates millimeter-wave system performance

\* PFNDAT contains phase functions, extinction and scattering coefficients, and the single-scattering albedo for 38 natural and man-made aerosols at 16 wavelengths ranging from 0.55 to 12.0  $\mu\text{m}$ . The single-scattering albedo is the ratio of the scattering coefficient to the extinction coefficient.

## References

---

1. J.T. Houghton and F.W. Taylor, "Remote sounding from artificial satellites and space probes of the atmospheres of the Earth and the planets," *Rep. Prog. Phys.*, 36, 827–919 (1973).
2. E.G. Njoku, "Passive microwave remote sensing of the Earth from space – a review," *Proc. IEEE*, 70(3), 728–750 (1982).
3. P.W. Rosenkranz et al., "Microwave radiometric measurements of atmospheric temperature and water from an aircraft," *J. Geophys. Res.*, 77(30), 5833–5844 (1972).
4. F.T. Ulaby, R.K. Moore, and A.K. Fung, *Microwave Remote Sensing Active and Passive*, Vol. III: *From Theory to Applications*, Artech House, Norwood, MA (1986).
5. N.C. Grody, "Surface identification using satellite microwave radiometers," *IEEE Trans. Geosci. Remote Sensing*, GE-26(6), 850–859 (1988).
6. T. Bellerby, M. Taberner, A. Wilmshurst, M. Beaumont, E. Barrett, J. Scott, and C. Durbin, "Retrieval of land and sea brightness temperatures from mixed coastal pixels in passive microwave data," *IEEE Trans. Geosci. Remote Sensing*, GE-36(6), 1844–1851 (Nov. 1998).
7. P.S. Chang and L. Li, "Ocean surface wind speed and direction retrievals from the SSM/I," *IEEE Trans. Geosci. Remote Sensing*, GE-36(6), 1866–1871 (Nov. 1998).
8. R.V. Engeset and D.J. Weydahl, "Analysis of glaciers and geomorphology on Svalbard using multitemporal ERS-1 SAR images," *IEEE Trans. Geosci. Remote Sensing*, GE-36(6), 1879–1887 (Nov. 1998).
9. N.J. Willis, *Bistatic Radar*, Artech House, Norwood, MA (1991).
10. A.O. Aboutalib and T.K. Luu, "An efficient target extraction technique for laser radar imagery," *Digital Signal Processing, Association, and Tracking of Point Source, Small, and Cluster Targets*, *Proc. SPIE* 1096 (1989).
11. J.M. Lloyd, *Thermal Imaging Systems*, Plenum Press, New York, NY (1982).
12. L.A. Klein, *Millimeter-wave and Infrared Multisensor Design and Signal Processing*, Artech House, Norwood, MA (1997).
13. J.A. Ratches, R.H. Vollmerhausen, and R.G. Driggers, "Target acquisition performance modeling of infrared imaging systems: Past, present, and future," *IEEE Sensors Journal*, Vol. 1, No. 1, 31–40 (June 2001).
14. D.L. Foiani and R.H. Pearce, "Combined radar and radiometer at millimeter wavelengths," *Symposium on Submillimeter Waves*, Polytechnic Institute of Brooklyn, Brooklyn, NY (March 1970).
15. V.G. Plank, R.O. Berthel, and B.A. Main, "Snow characterization measurements and E/O correlation obtained during Snow-One-A and Snow-One-B," *Proc. SPIE* 414, 97–102, (1983).
16. G.W. Aitken, Ed., *Snow-One-A Data Report*, Special Report 82-8, AD B068569L, U.S. Army Cold Regions Research and Engineering Laboratory/CRREL-RG, Hanover, NH (May 1982).



17. M.A. Seagraves and J.F. Ebersole, "Visible and infrared transmission through snow," *Opt. Eng.*, 22(1), 90–93 (Jan.-Feb. 1983).
18. V.J. Falcone Jr., L.W. Abreu, and E.P. Shettle, *Atmospheric Attenuation of Millimeter and Submillimeter Waves: Models and Computer Code*, AFGL-TR-79-0253 (AD A084485), Air Force Geophysics Laboratory, Hanscom AFB, MA (Oct. 1979).
19. F.T. Ulaby, R.K. Moore, and A.K. Fung, *Microwave Remote Sensing: Active and Passive*, Vol. I: *Microwave Remote Sensing Fundamentals and Radiometry*, Artech House, Norwood, MA (1981).
20. R.K. Parker and R.H. Abrams, Jr., "Radio frequency vacuum electronics: A resurgent technology for tomorrow," *Millimeter-Wave Technology IV and Radio Frequency Power Sources*, *Proc. SPIE* 791, 2–12 (1987).
21. R.K. Crane, *Microwave Scattering Parameters for New England Rain*, Technical Report 426, Lincoln Laboratory, MIT (Oct. 3, 1966).
22. J. Nemarich, R.J. Wellman, and J. Lacombe, "Backscatter and attenuation by falling snow and rain at 96, 140, and 225 GHz," *IEEE Trans. Geosci. Remote Sensing*, GE-26(3), 319–329 (1988).
23. H. Goldstein, "Attenuation by condensed water," Chapter 8 in *Propagation of Short Radio Waves*, in D.E. Kerr (ed.), McGraw-Hill, New York, NY (1951).
24. D. Atlas, "Advances in radar meteorology," in *Advances in Geophysics*, Vol. 10, 317–478, Academic Press, New York, NY (1964).
25. A.J. Bogush, Jr., *Radar and the Atmosphere*, Artech House, Norwood, MA (1989).
26. R.K. Crane, "Prediction of attenuation by rain," *IEEE Trans. Comm.*, COM-28(9), 1717–1733 (Sept. 1980).
27. V.J. Falcone, Jr. and L.W. Abreu, "Atmospheric attenuation of millimeter and submillimeter waves," *IEEE EASCON-79 Conference Record*, Vol. 1, pp. 36–41 and *Millimeter Wave Radar*, S.L. Johnston, Editor, Artech House, Norwood, MA (1980).
28. V.W. Richard, J.E. Kammerer, and R.G. Reitz, *140 GHz Attenuation and Optical Visibility Measurements of Fog, Rain, and Snow*, ARBRL-MR-2800 (1977).
29. K.A. Richer, "Environmental effects on radar and radiometric systems at millimeter wavelengths," A72-15610, *Proc. Symposium on Submillimeter Waves*, Polytechnic Institute of Brooklyn, Brooklyn, NY, 533–543 (Mar. 31–Apr. 2, 1970).
30. H.B. Wallace, "Millimeter-wave propagation measurements at the Ballistic Research Laboratory," *IEEE Trans. Geosci. Remote Sensing*, GE-26(3), 253–258 (1988).
31. V.I. Rozenberg, "Radar characteristics of rain in submillimeter range," *Radio Eng. and Electron. Phys.*, 15(12), 2157–2163 (1970).

32. R.K. Crane, "Propagation phenomena affecting satellite communication systems operating in the centimeter and millimeter wavelength bands," *Proc. IEEE*, 59, 173–188 (1971).
33. V.W. Richard, J.E. Kammerer, and H.B. Wallace, "Rain backscatter measurements at millimeter wavelengths," *IEEE Trans. Geosci. Remote Sensing*, GE-26(3), 244–252 (1988).
34. R.D. Hudson, *Infrared System Engineering*, John Wiley and Sons, New York, NY (1969).
35. H. Weichel, *Laser Beam Propagation in the Atmosphere*, Vol. TT3, SPIE Optical Engineering Press, Bellingham, WA (1990).
36. A.J. LaRocca, "Methods of calculating atmospheric transmittance and radiance in the infrared," *Proc. IEEE*, 63(1), 75–94 (Jan. 1975).
37. F.X. Kneizys, E.P. Shettle, W.O. Gallery, J.H. Chetwynd Jr., L.W. Abreu, J.E.A. Selby, R.W. Fenn, and R.A. McClatchey, *Atmospheric Transmittance/Radiance: Computer Code LOWTRAN 5*, AFGL-TR-80-0067, AFGL, Hanscom AFB, MA 01731 (1980).
38. F.X. Kneizys, E.P. Shettle, W.O. Gallery, J.H. Chetwynd Jr., L.W. Abreu, J.E.A. Selby, S.A. Clough, and R.W. Fenn, *Atmospheric Transmittance/Radiance: Computer Code LOWTRAN 6*, AFGL-TR-83-0187, AFGL, Hanscom AFB, MA 01731 (1983).
39. F.X. Kneizys, E.P. Shettle, L.W. Abreu, J.H. Chetwynd Jr., G.P. Anderson, W.O. Gallery, J.E.A. Selby, and S.A. Clough, *Users Guide to LOWTRAN 7*, AFGL-TR-88-0177, AFGL, Hanscom AFB, MA 01731 (1988).
40. P.W. Kruse, L.D. McGlauchlin, and R.B. McQuistan, *Elements of Infrared Technology*, John Wiley and Sons, New York, NY (1962).
41. H.A. Brown and B.A. Kunkel, "Water vapor, precipitation, clouds, and fog," Section 4 of Chapter 16 in A.S. Jursa (ed.), *Handbook of Geophysics and the Space Environment*, AFGL-TR-85-0315 (AD A167000), USAF Geophysics Laboratory, Hanscom AFB, MA 01731 (1985).
42. W.R. Watkins, F.T. Kantrowitz, and S.B. Crow, "Optical, infrared, and millimeter wave propagation engineering," *Proc. SPIE* 926, 69–84 (1988).
43. *Smoke and Natural Aerosol Parameters (SNAP) Manual*, Joint Technical Coordinating Group for Munitions Effectiveness, Smoke and Aerosol Working Group, Report 61, JTCG/ME-85-2 (Apr. 26, 1985).
44. R.W. Fenn, S.A. Clough, W.O. Gallery, R.E. Good, F.X. Kneizys, J.D. Mill, L.S. Rothman, E.P. Shettle, and F.E. Volz, "Optical and infrared properties of the atmosphere," Chapter 18 in A.S. Jursa (ed.), *Handbook of Geophysics and the Space Environment*, AFGL-TR-85-0315 (AD A167000), USAF Geophysics Laboratory, Hanscom AFB, MA 01731 (1985).
45. A. Berk, L.S. Bernstein, and D.C. Robertson, *MODTRAN: A Moderate Resolution Model for LOWTRAN 7*, GL-TR-89-0122, USAF Geophysics Laboratory, Hanscom AFB, MA 01731 (1989).
46. L.S. Rothman, et al., "The HITRAN molecular database: Editions of 1991 and 1992," *J. Quant. Spectrosc. Radiat. Transfer*, 28, 469 (1992).

47. G.P. Anderson, J.H. Chetwynd, J.M. Theriault, P. Acharya, A. Berk, D.C. Robertson, F.X. Kneizys, M.L. Hoke, L.W. Abreu, and E.P. Shettle, "MODTRAN 2: Suitability for remote sensing," *Atmospheric Propagation and Remote Sensing II, Proc. SPIE* 1968, 514–525 (1993).
48. P.K. Acharya, D.C. Robertson, and A. Berk, *Upgraded Line-of-Sight Geometry Package and Band Model Parameters for MODTRAN*, Phillips Laboratory Technical Report PL-TR-93-2127, Geophysics Directorate, Hanscom AFB, MA 01731 (1993).
49. A. Berk, *Upgrades to the MODTRAN Layer Cloud/Rain Models*, Report SSI-SR-56, Spectral Sciences, Inc., Burlington, MA (1995).
50. J.H. Chetwynd, J. Wang, and G.P. Anderson,, "FASCODE: An update and applications in atmospheric remote sensing," *Proc. SPIE* 2266, 613–623 (1994).
51. J. Wang, G.P. Anderson, H.E. Revercomb, and R.O. Knutseon, "Validation of FASCODE 3 and MODTRAN 3: Comparison of model calculations with ground-based and airborne interferometer observations under clear sky conditions," *Appl. Op.*, 35(30), 6028–6040 (Oct. 1996).
52. L.S. Bernstein, A. Berk, D.C. Robertson, P.K. Acharya, G.P. Anderson, and J.H. Chetwynd, "Addition of a correlated-k capability to MODTRAN," *Proc. 19<sup>th</sup> Annual Conf. on Atmospheric Transmission Models*, Phillips Laboratory, Geophysics Directorate, Hanscom AFB, MA 01731 (Jun. 1996).
53. R.C. Shirkey, "Effects of atmospheric and man-made obscurants on visual contrast," *Atmospheric Effects on Systems Performance, Proc. SPIE* 305, 37–44 (1981).
54. R.C. Shirkey, L.D. Duncan, and F.E. Niles, *EOSAEL 87, Vol. 1, Executive Summary*, Rpt. TR-0221-1, U.S. Army Laboratory Command, Atmospheric Sciences Laboratory, White Sands Missile Range, NM 88002-5501 (Oct. 1987).
55. *Night Vision Laboratory Static Performance Model for Thermal Viewing Systems*, ECOM Report 7043, AD A011212 (Apr. 1975).
56. L. Scott and L. Conduff, "CNVEO advanced FLIR systems performance model," *Proc. SPIE* 1309, Paper 17 (Apr. 1990).
57. H.V. Kennedy, "Modeling second generation thermal imaging sensors," *Proc. SPIE* 1309, Paper 1 (Apr. 1990).